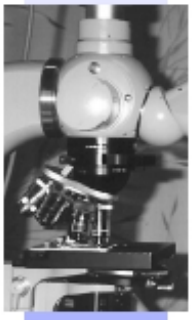
SINGLE REFLECTION AT CURVILINEAR INTERFACES

The *Tip Wave Superposition Method* using an effective reflection coefficient

by

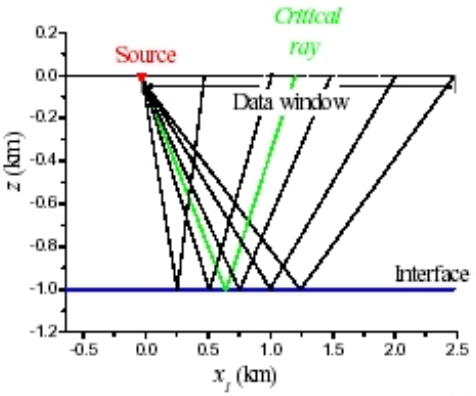
A.M. Aizenberg, M.A. Aizenberg, H.B. Helle,

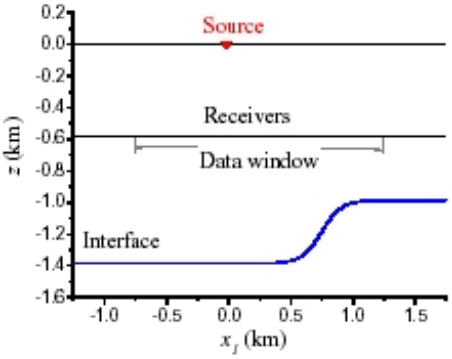
K.D. Klem-Musatov and J. Pajchel

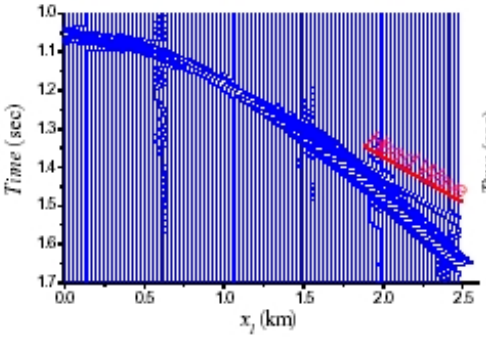


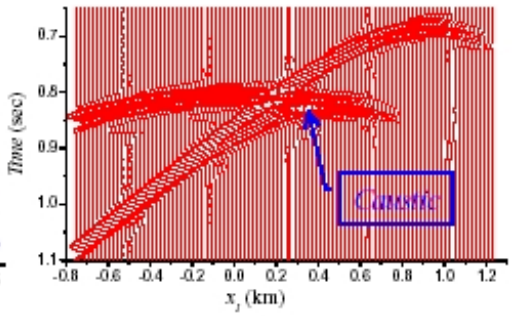












E&P
Research centre Bergen

December, 2002

SINGLE REFLECTION AT CURVILINEAR INTERFACES

The Tip Wave Superposition Method using an effective reflection coefficient

by

Arkady M. Aizenberg*, Milana A. Aizenberg**, Hans B. Helle***,
Kamill D. Klem-Musatov*, Jan Pajchel***

** Institute of Geophysics, Russian Academy of Science, Novosibirsk, Russia*

*** Institute of Geophysics, Russian Academy of Science,*
and Novosibirsk State University, Novosibirsk, Russia

**** E&P Research Centre, Norsk Hydro asa, Bergen, Norway*

Novosibirsk and Bergen, December, 2002.

Summary

This report summarizes the results of numerical tests of an improved algorithm for computing synthetic seismograms in 3-D models based on the Tip Wave Superposition Method (TWSM). Compared with earlier versions of TWSM the improvements comprise a generalization of the background theory that also accounts for wave phenomena at critical reflections (headwaves) and the replacement of the plane-wave reflection coefficient with an effective coefficient that eliminates diffraction artefacts at critical angles. The results presented in this report were essentially obtained during the stay of Milana Aizenberg (Novosibirsk) as a trainee student at Norsk Hydro, E&P Research Centre (Bergen) during August-September 2002.

Introduction

Seismic wavefield simulation algorithms are developed so that they allow for inversion of the model parameters [6, 12]. The purpose of such algorithms is to represent the wavefield in the form of isolated wave events, which can be directly identified with elements of the geophysical model. To provide this possibility, the Tip Wave Superposition Method (TWSM) was introduced for simulation of the 3-D wavefield scattered by curvilinear interfaces [2, 8]. However, in the initial approach the wavefield at an interface was described by using the plane-wave reflection/transmission coefficients which are discontinuous at critical angles. This implies that instead of creating headwaves at critical angles the TWSM produces artefacts in the form of edgewaves diffracted from the contours formed by the critical points on the interface. Similar artefacts were discussed in detail in [11, 13]. To develop a theoretical foundation of the method based on the Helmholtz integral, we introduced in [9] a solution of the scalar transmission problem for a curvilinear interface between inhomogeneous layers in the form of a composition of propagator and transmitter matrices, where the elements can be expressed in terms of the classical surface potentials and an, initially unknown, matrix reflection/transmission operator. In [3-5] the scalar elements of the reflection/transmission matrix were converted to the form of effective reflection/transmission coefficients in the case of a plane interface between homogeneous layers.

In this report we first present a short introduction to the theory and the numerical implementation of the TWSM using the effective reflection coefficient for the 3-D wavefield scattered from a curvilinear interface. In Section 1 we describe the model of the medium and state the problem of scalar wavefield scattering. In Section 2 we provide the exact representation of the single scattered wavefield. In Section 3 we introduce the approximate description of the single scattered wavefield in terms of TWSM, but substituting the plane wave reflection coefficients with the effective reflection coefficient. In Section 4 we discuss the accuracy of the TWSM seismogram obtained with the effective reflection coefficient compared with the analytical solution obtained in the case of a plane reflector. In Section 5 we compare the TWSM seismograms obtained with the effective and plane-wave reflection coefficients for a range of interface geometries. In Section 6 we demonstrate the formation of the headwave caustics by the concave part of an interface using the TWSM approach.

1. Scattering from a smooth curvilinear interface between homogeneous layers

We consider scalar non-stationary scattering from an infinite smooth interface Σ between homogeneous half-spaces Ω_1 and Ω_2. Let c_j be the wave propagation velocity in the half-space Ω_j ($j=1,2$). We assume that the interface Σ has a plane infinite extent and a local curvilinear perturbation of finite extent. The correct statement of this problem in the general case is given in [10, 14]. All the formulas below are given for stationary wavefields as functions of the angular frequency ω. Non-stationary wavefields are obtained using the Fourier transform. Let the vector $\mathbf{R}$ designate any point of space, and vectors $\mathbf{r}$ and $\mathbf{r}_0$ designate points on the interface. Let a point source be located in the half-space Ω_1. This source generates the diverging spherical wave $d_1(\mathbf{R})$ with the pulse form (see Figure 1)

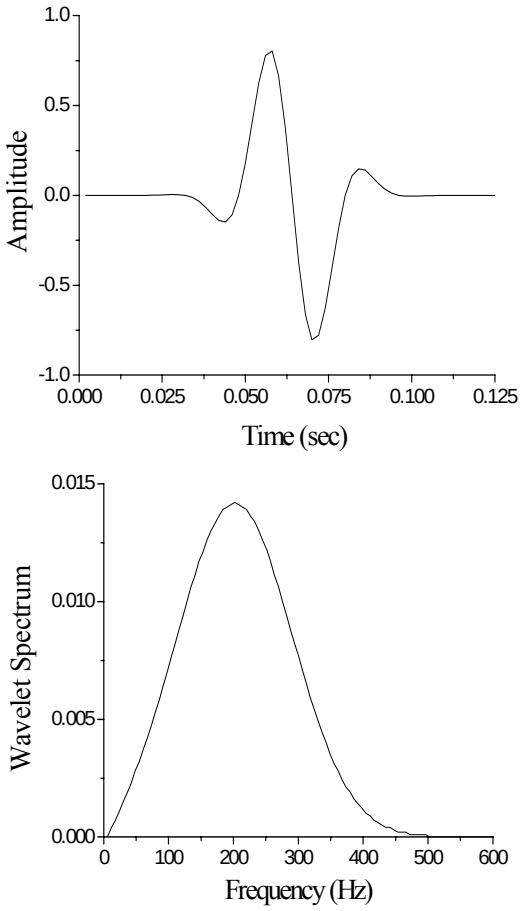


Figure 1: The wavelet and its spectrum

$$F(t) = -\exp\left(-p^2/\pi^2\right)\sin(p), \quad p = 2\pi\frac{(t-t_0)}{T},$$

where $t_0 = 0.064$ sec is a time shift for the central point of the pulse, $T = 0.032$ sec is the dominant wave period.

As the result of scattering of the wave $d_1(\mathbf{R})$ by the interface, the scattered wavefield $s_j(\mathbf{R})$ arises in each half-space Ω_j. Therefore the complete wavefield in the half-space Ω_1 can be represented by the sum $d_1(\mathbf{R}) + s_1(\mathbf{R})$, and the complete wavefield in the half-space Ω_2 coincides with $s_2(\mathbf{R})$. The scattered wavefield satisfies the wave equation

$$\left[\nabla^2 + \omega^2/c_j^2\right] s_j(\mathbf{R}) = 0 \tag{1}$$

The traces of the complete wavefield and its normal derivative satisfy the transmission conditions at Σ

$$d_1(\mathbf{r}) + s_1(\mathbf{r}) = s_2(\mathbf{r}), \quad \frac{1}{\rho_1}\left[\partial d_1(\mathbf{r})/\partial n + \partial s_1(\mathbf{r})/\partial n\right] = \frac{1}{\rho_2}\,\partial s_2(\mathbf{r})/\partial n, \tag{2}$$

where ρ_j is density in the half-space Ω_j, $\mathbf{n}$ is the unit vector normal to Σ and directed into Ω_1.

2. Single scattered wavefield

Here we consider the single scattered wavefield $s_1^{(1)}(\mathbf{R})$ being part of the scattered wavefield $s_1(\mathbf{R})$ and use the corresponding formulas obtained in [9]. The single scattered wavefield $s_1^{(1)}(\mathbf{R})$ can be expressed through the action of the composite propagation operator $P_1(\mathbf{R}, \mathbf{r}_0)$ on the traces of the reflected wavefield $r_1^{(1)}(\mathbf{r}_0)$ and its normal derivative $\partial r_1^{(1)}(\mathrm{r}_0)/\partial n$ given at the interface Σ

$$s_1^{(1)}(\mathbf{R}) = P_1(\mathbf{R}, \mathbf{r}_0)\left\{r_1^{(1)}(\mathbf{r}_0), \partial r_1^{(1)}(\mathbf{r}_0)/\partial n\right\}. \tag{3}$$

The boundary value $r_1^{(1)}(\mathbf{r}_0)$ describes the wavefield locally reflected at the point $\mathbf{r}_0$ of the interface. The scattered wavefield $s_1^{(1)}(\mathbf{R})$ represents superposition of the wavefields coming from the different reflection points. The limiting value $s_1^{(1)}(\mathbf{r}_0)$ does not in general coincide with the boundary value $r_1^{(1)}(\mathbf{r}_0)$. Values of the traces $r_1^{(1)}(\mathbf{r}_0)$ and $\partial r_1^{(1)}(\mathbf{r}_0)/\partial n$ at any chosen point $\mathbf{r}_0$ of the interface can be expressed through the traces of the source wavefield $d_1(\mathbf{r})$ and its normal derivative $\partial d_1(\mathbf{r})/\partial n$

$$r_1^{(1)}(\mathbf{r}_0) = K_{11}(\mathbf{r}_0, \mathbf{r})\, d_1(\mathbf{r}), \quad \partial r_1^{(1)}(\mathbf{r}_0)/\partial n = -K_{11}(\mathbf{r}_0, \mathbf{r})\, \partial d_1(\mathbf{r})/\partial n \tag{4}$$

using the reflection operator

$$K_{11}(\mathbf{r}_0, \mathbf{r}) = \mathbb{F}^{-1}(\mathbf{r}_0, \zeta)\, k_{11}(\zeta)\, \mathbb{F}(\zeta, \mathbf{r}). \tag{5}$$

The space Fourier operator $\mathbb{F}(\zeta, \mathbf{r})$ transforms the traces $d_1(\mathbf{r})$ and $\partial d_1(\mathbf{r})/\partial n$ from the curvilinear interface coordinates $\mathbf{r} = (x_1, x_2)$ into the wave number domain $\zeta = (\zeta_1, \zeta_2)$. The inverse Fourier operator $\mathbb{F}^{-1}(\mathbf{r}_0, \zeta)$ provides the value at the origin $\mathbf{r}_0 = (0, 0)$ of the interface

coordinates. The kernel $k_{11}(\zeta)$ of the operator (5) coincides with the plane-wave reflection coefficient.

3. TWSM with effective reflection coefficient

It can be shown that in the limiting case $\omega \to \infty$ the composite propagation operator $P_1(\mathbf{R}, \mathbf{r}_0)$ tends to the Helmholtz integral operator. That is why we compute the single scattered wavefield $s_1^{(1)}(\mathbf{R})$ in the TWSM, and in [1, 2, 8] we introduced an approximate propagation operator $P_1^{TWSM}(\mathbf{R}, \mathbf{r}_0)$ and suggested that one should evaluate the approximate single scattered wavefield by the formula

$$s_1^{(1)TWSM+PWC}(\mathbf{R}) = P_1^{TWSM}(\mathbf{R}, \mathbf{r}_0)\, \chi_{11}^{PWC}(\mathbf{r}_0)\, d_1(\mathbf{r}_0) \tag{6}$$

using the plane-wave reflection coefficient $\chi_{11}^{PWC}(\mathbf{r}_0)$. Then the single scattered wavefield $s_1^{(1)}(\mathbf{R})$ can be represented by

$$s_1^{(1)}(\mathbf{R}) = s_1^{(1)TWSM+PWC}(\mathbf{R}) + \delta s_1^{(1)HI}(\mathbf{R}) + \delta s_1^{(1)PWC}(\mathbf{R}), \tag{7}$$

where the error term $\delta s_1^{(1)HI}(\mathbf{R})$ is due to the approximation imbedded in the Helmholtz integral, and the error term $\delta s_1^{(1)PWC}(\mathbf{R})$ is due to the application of the plane-wave reflection coefficient instead of the reflection operator $K_{11}(\mathbf{r}_0, \mathbf{r})$. Notice, however, that in general the error term $\delta s_1^{(1)PWC}(\mathbf{R}) \neq 0$ even for a plane reflector.

Numerical tests have revealed that for the TWSM algorithm, using the plane-wave reflection coefficient, the error $\delta s_1^{(1)PWC}(\mathbf{R})$ has the form of diffraction artefacts generated at the locus of critical reflection on the interface. As well known [11, 13] all superposition methods based on the Helmholtz integral and the plane-wave reflection coefficient, imply artefacts of this type. This is why the plane-wave reflection coefficient $\chi_{11}^{PWC}(\mathbf{r}_0)$ is insufficient to model wide-angle reflection phenomena by superposition methods. Using the reflection operator $K_{11}(\mathbf{r}_0, \mathbf{r})$ instead of the plane-wave reflection coefficient remedies this deficiency and completely eliminates the error term $\delta s_1^{(1)PWC}(\mathbf{R})$. We thereby smooth the amplitude across the critical points and add headwaves to obtain a more complete and realistic seismic response.

It can be shown that the actual trace of the source wavefield $d_1(\mathbf{r})$ can be approximated by the trace of a spherical wave given at the plane tangent to the interface at a point $\mathbf{r}_0$. Then the trace $r_1^{(1)}(\mathbf{r}_0)$ in (4) can be expressed in terms of the effective reflection coefficient $\chi_{11}^{EC}(\mathbf{r}_0)$ by

$$r_1^{(1)}(\mathbf{r}_0) = \chi_{11}^{EC}(\mathbf{r}_0)\, d_1(\mathbf{r}_0) + \delta r_1^{(1)}(\mathbf{r}_0), \tag{8}$$

where $\delta r_1^{(1)}(\mathbf{r}_0)$ is error due to the approximation in the reflection operator $K_{11}(\mathbf{r}_0, \mathbf{r})$.

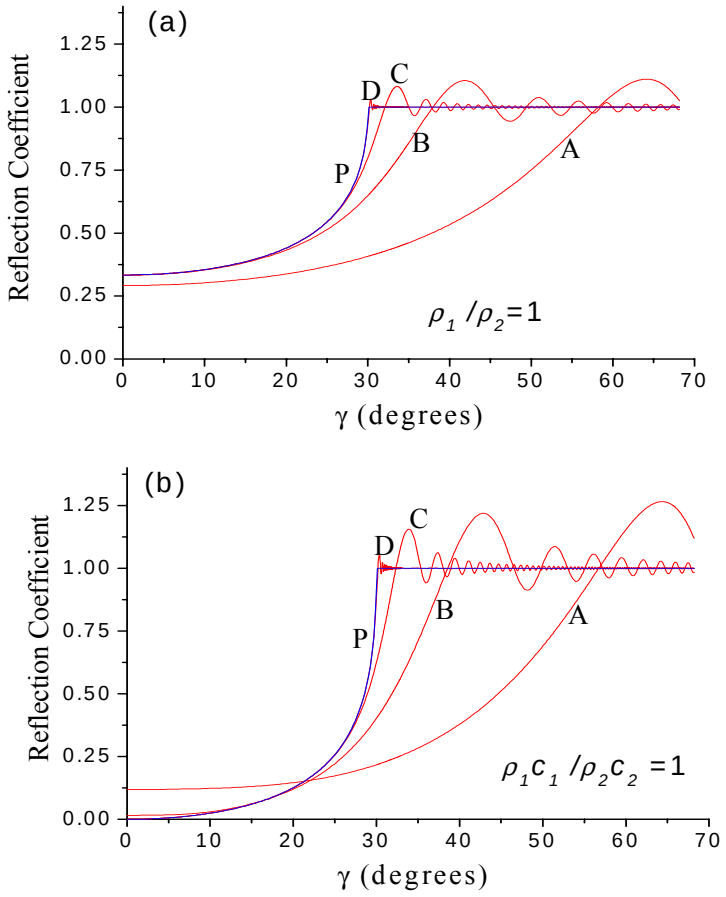


Figure 2: Comparison of plane wave reflection coefficient (P) with the effective reflection coefficients for various values of kh (A: kh=10, B: kh=100, C: kh=1000). In (a) we set ρ_1/ρ_2 =1 and (b) $\rho_1 c_1/\rho_2 c_2$ =1 (no impedance contrast).

The effective reflection coefficient $\chi_{11}^{EC}(\mathbf{r}_0)$ was introduced in [3, 4] to describe reflection of a spherical wave from a plane interface between homogeneous half-spaces. The derivation of this coefficient in the case of a curvilinear interface will be published in a separate paper. In [5] the effective reflection coefficient $\chi_{11}^{EC}(\mathbf{r}_0)$ was expressed by a smooth function of four dimensionless parameters: density ratio ρ_1/ρ_2, velocity ratio c_1/c_2, angle of incidence γ and parameter kh, where h is the distance between the source and the tangent plane and k is the wave number defined by $k = \sqrt{(\omega/c_1)^2 + (\omega/c_2)^2}$.

Figure 2 displays the effective reflection coefficient as a function of incidence angle γ for a range of values of kh (red curves). The plane-wave reflection coefficient (blue curve) is shown for comparison. In case (a) the two layers have the same density ($\rho_1/\rho_2 = 1$) but contrast in velocity ($c_1/c_2 = 0.5$). We observe that the modulus of effective reflection coefficient approaches that of the plane-wave for $k\,h \to \infty$. The oscillatory behaviour at supercritical angles reflects the interference between the reflected and headwave events [5]. While a high-frequency spherical wave (D) clearly detects a jump at the critical angle, the amplitude of a low-frequency wave (A) varies smoothly with γ. Similar features are apparent from Figure 2b where the model parameters are adjusted such that $\rho_1 c_1/\rho_2 c_2 = 1$, i.e. no plane-wave impedance contrast exists for $\gamma = 0$ and hence there is a zero

reflection coefficient for small angles. We notice, however, that the latter applies to plane waves and spherical waves of high frequencies (B-D) whereas the low-frequency wave (A) still reveals a significant reflection coefficient at $\gamma = 0$.

By substituting (8) in (6), we obtain

$$s_1^{(1)}(\mathbf{R}) = s_1^{(1)TWSM+EC}(\mathbf{R}) + \delta s_1^{(1)HI}(\mathbf{R}) + \delta s_1^{(1)EC}(\mathbf{R}), \tag{9}$$

where the single scattered wavefield computed by the TWSM algorithm is

$$s_1^{(1)TWSM+EC}(\mathbf{R}) = P_1^{TWSM}(\mathbf{R}, \mathbf{r}_0)\, \chi_{11}^{EC}(\mathbf{r}_0)\, d_1(\mathbf{r}_0), \tag{10}$$

and the error $\delta s_1^{(1)EC}(\mathbf{R})$ is due to using the effective reflection coefficient instead of the reflection operator $K_{11}(\mathbf{r}_0, \mathbf{r})$. It is evident that the error $\delta s_1^{(1)EC}(\mathbf{R}) = 0$ for a plane interface.

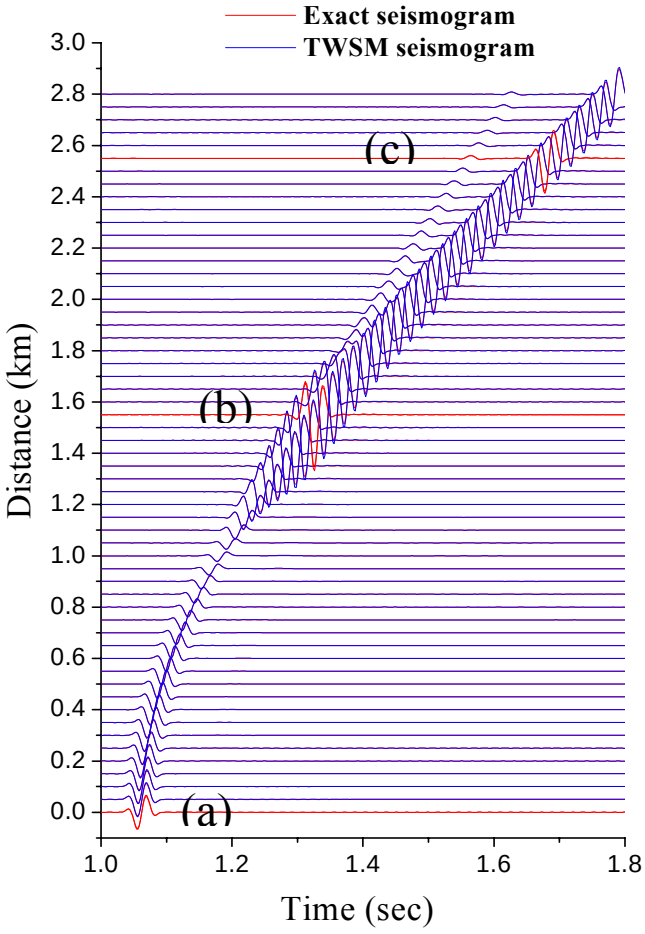


Figure 3: Comparison of TWSM seismograms (blue) with the exact solution (red) for a plane interface. See Figure 4 for details at the receiver location (a), (b) and (c).

4. Comparison of TWSM seismograms with the analytical solution for a plane interface.

We begin with estimation of the error $\delta s_1^{(1)HI}(\mathbf{R})$ in (7) and (9). For this purpose it is sufficient to compare the TWSM seismogram obtained by formula (10) with the exact seismogram in case of a plane interface between two homogeneous media when the error $\delta s_1^{(1)EC}(\mathbf{R})$ is absent. For simplicity, we introduce the Cartesian coordinate system (x_1, x_2, z) with the source located in its origin.

A comparison of the TWSM algorithm with the exact modelling is made for the interface given by the expression $z = -1$ km. Here we

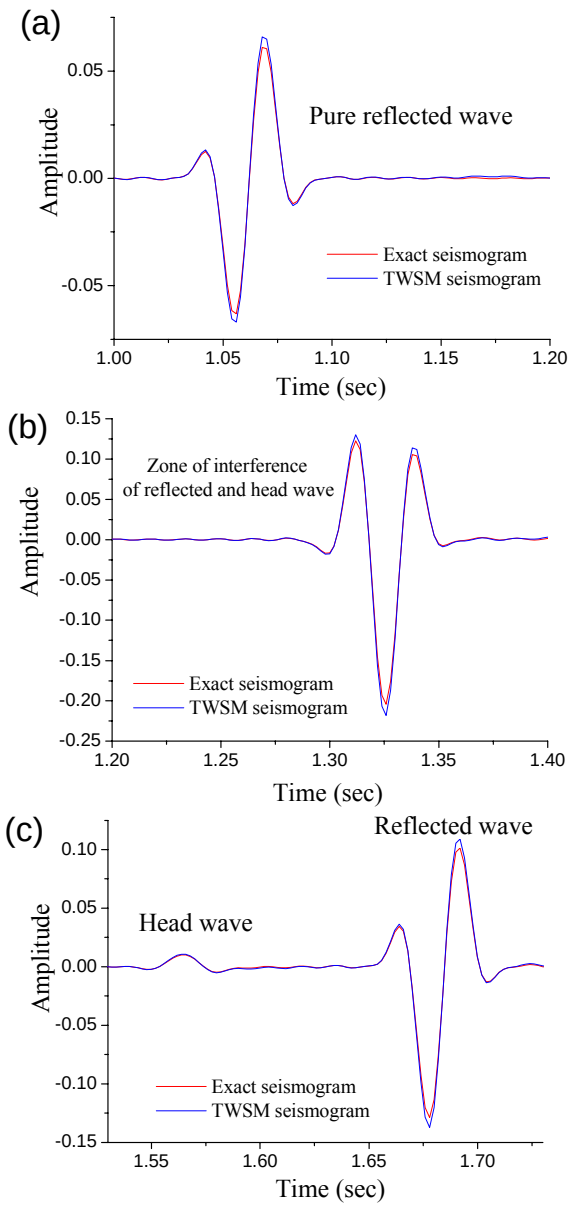


Figure 4: Details of the seismic traces (Figure 3) at offsets of 0 (a), 1.55 km (b) and 2.55 km (c).

consider a density ratio $\rho_1/\rho_2 = 1$ and velocities $c_1 = 2$ km/s and $c_2 = 4$ km/s. Let the 57 receivers be horizontally distributed at intervals 0.05 km from the source. Figure 3 shows both the TWSM seismogram (in blue) and the analytical solution (in red). Visual inspection reveals minor differences between the two seismograms. Therefore we provide a more detailed comparison in Figure 4, at three separate receiver locations as indicated in Figure 3. In general the TWSM peak amplitudes are negligibly higher than those of the analytical solution, for sub-critical angles (a), critical (b) as well as in the super-critical range (c). Numerical comparison with the plane interface model has revealed a small error of almost constant value, apparently independent of the source-receiver distance. All the numerical tests performed with the TWSM software indicate a relative error in amplitude of less than 9%. For a curvilinear interface we have not yet estimated the error $\delta s_1^{(1)EC}(\mathbf{R})$ since the computation of the single reflected wavefield by the exact formula (4) remains to be implemented.

5. Comparison of TWSM seismograms using effective and plane-wave coefficients

The main goal of the numerical tests is to demonstrate the advantage of using the effective coefficients. For this purpose it is sufficient to compute the single reflected wavefield using the formulas (6) and (10) for a selection of simple interface geometries.

Here we will demonstrate the advantage of using the effective reflection coefficient instead of the plane-wave reflection coefficient applied in evaluating the reflected wavefield and its normal derivative. The use of the plane-wave reflection coefficient is, however, not feasible at critical angles because of the discontinuities in the reflected wavefield, implying that the

Helmholtz propagator $H_1(\mathbf{R},\mathbf{r}_0)$ or the TWSM propagator $P_1^{TWSM}(\mathbf{R},\mathbf{r}_0)$ introduce artefacts in the form of edgewaves. These effects form the error $\delta s_1^{(1)PWC}(\mathbf{R})$ that is clearly visible on synthetic seismograms evaluated by the plane-wave coefficient (see also Introduction of [11]).

The TWSM algorithm with the effective reflection coefficient was tested on several types of interfaces with constant density contrast $\rho_1/\rho_2=1$ but a range of velocity contrasts. In the following sections we perform numerical tests on four different models in order to evaluate the difference between the plane-wave and effective coefficients in the seismograms obtained using the TWSM algorithm.

As for other grid-based numerical methods of wave propagation the grid has a finite extent and thus numerical artefacts may arise at the numerical mesh boundaries. In the present case the mesh boundaries are the edges of the interface, which are curves of discontinuity in properties and hence the TWSM algorithm will produce edge diffractions as expected. However, these are the common numerical artefacts due to model truncation. They are normally unwanted, and thus should be eliminated. Here we have introduced a tapering zone of width 30 grid points (rectangular grid of size 10 m) where the reflection coefficient is smoothly damped to zero using damping functions of the form

$$f(x_1,x_2)=1+\left(\frac{c_2}{c_1}-1\right)\xi^+(x_1)\xi^-(x_1)\eta^+(x_2)\eta^-(x_2),$$

where

$$\xi^\pm(x_1)=\frac{1}{1+\exp\left\{\pm A\left(x_1^\pm-x_1\right)\right\}},\quad \eta^\pm(x_2)=\frac{1}{1+\exp\left\{\pm A\left(x_2^\pm-x_2\right)\right\}},$$

are sigmoid functions and $x_1^\pm$ are coordinates of the central lines of two rectangular strips parallel to the x_2 axis, and $x_2^\pm$ are coordinates of central lines of two rectangular strips parallel to the x_1 axis. A constant $A=10$ is chosen under the conditions $f(x_1,x_2)=c_2/c_1$ at the external edge of absorbing strip and $f(x_1,x_2)=1$ at the internal edge. The effective and plane-wave reflection coefficients are computed using the auxiliary velocity in the upper half-space $c_1 f(x_1,x_2)$.

Along with the seismograms, figures showing the corresponding models are provided. Although the models and the wavefields are in 3-D, the pictures are drawn as 2-D sections for simplicity.

Test 1. The first test is made for a horizontal plane interface given by $z=-1\,\text{km}$. We consider the velocities $c_1=2\,\text{km/s}$ and $c_2=4\,\text{km/s}$. As it is shown on Figure 5a, the receivers

are distributed at intervals of 0.025 km in the level $z = 0$ with the first receiver in the source point, sufficiently far from the absorbing boundaries. Figure 5b shows the cosine of the incidence angle γ along the receiver profile. The intersection between the cosines of critical incidence angle $\gamma_{critical}$ and γ correspond to points of critical rays. As seen from Figure 5b the critical points form a circle on the horizontal interface, with a radius 0.566 km and centred at the source foot point. Figure 5c shows the seismograms obtained by the TWSM algorithm using the plane-wave reflection coefficient. This seismogram includes pure reflected wave and the artificial diffraction along the contour of critical reflection. Using the effective reflection coefficient (c), on the other hand, the diffraction artefacts are completely removed and a

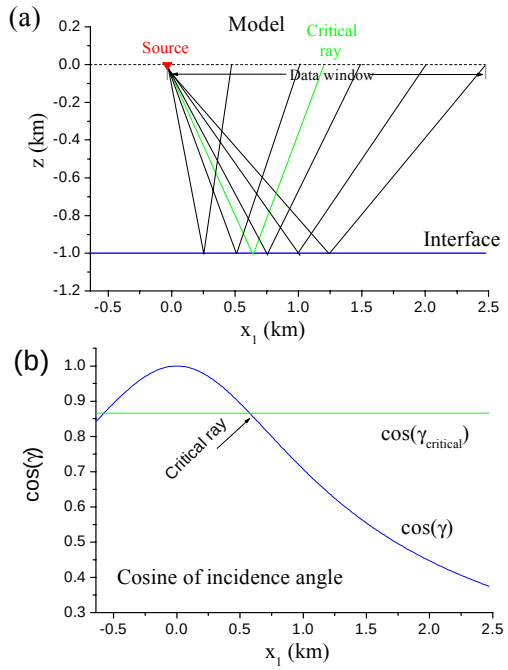


Figure 5: Reflection at a plane interface (Test 1).

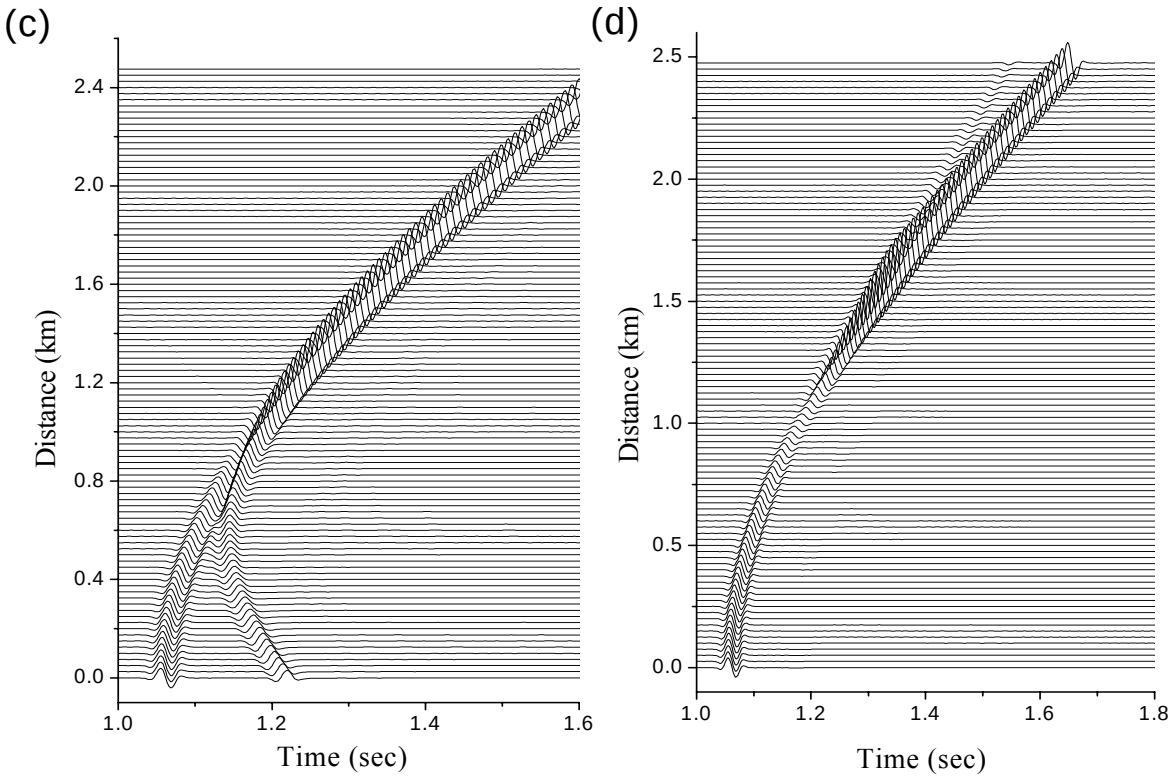


Figure 5 (cont.): Comparison of seismograms obtained using the plane-wave reflection coefficient (c) and the effective reflection coefficient (d) in the plane interface model (a,b). (Test 1)

headwave appears.

Test 2. The TWSM algorithm is tested for a locally curvilinear interface of syncline type with a significant deviation from the plane. We consider the same velocities as in the previous experiment. The interface is given by the expression $z = -1 - 0.3\exp\left\{-16\left(x_1^2 + x_2^2\right)\right\}$ km, which allows each point of the interface to be exposed both from the source and receivers. The receivers are distributed at intervals of 0.02 km in the level $z = 0$. Figures 6a and 6b show a section through the model and the graph of cosine of the incidence angles, respectively. In this particular case we observe that three circles formed by the critical points on the interface,

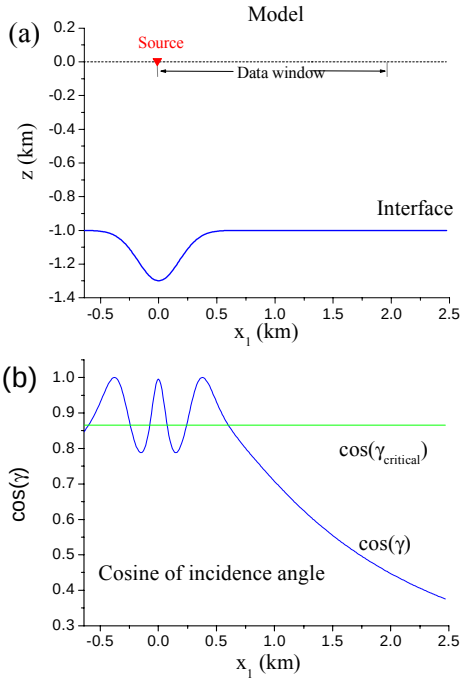


Figure 6: Reflection at an interface with a syncline (Test 2).

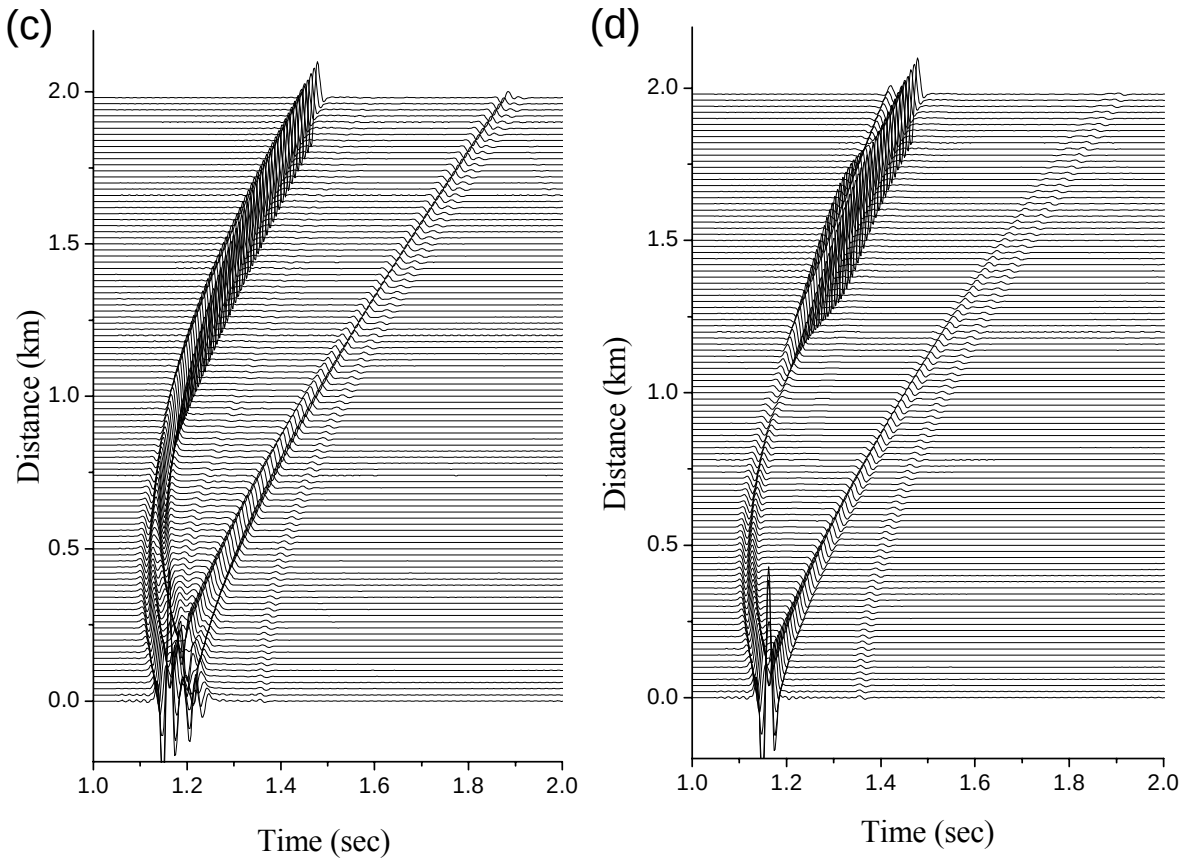


Figure 6 (cont.): Comparison of seismograms obtained using the plane-wave reflection coefficient (c) and the effective reflection coefficient (d) in the syncline interface model (a,b) (Test 2).

with the centres in the source foot point and radii 0.075 , 0.242 and 0.566 km implying that three critical angles exist at either side of the symmetry axis along the section Figure 6. The TWSM response using the plane-wave and effective reflection coefficients are shown in Figures 6c and 6d, respectively.

The strongest event is the reflection from the part of interface between the foot point (normal incidence) at $x_1 = 0.381$ km and about $x_1 = 1$ km. The weaker loop-like events are reflections from the syncline part of the interface between two points of normal incidence at $x_1 = -0.381$ km and $x_1 = 0$. In fact, these two events are branches of a triplication with focal point at $x_1 = 0$.

A headwave from the plane part of the interface at $0.566 < x_1 < 1.0$ km is recorded by the receivers for $x_1 \geq 1.2$ km (d). A corresponding artificial edge diffraction is

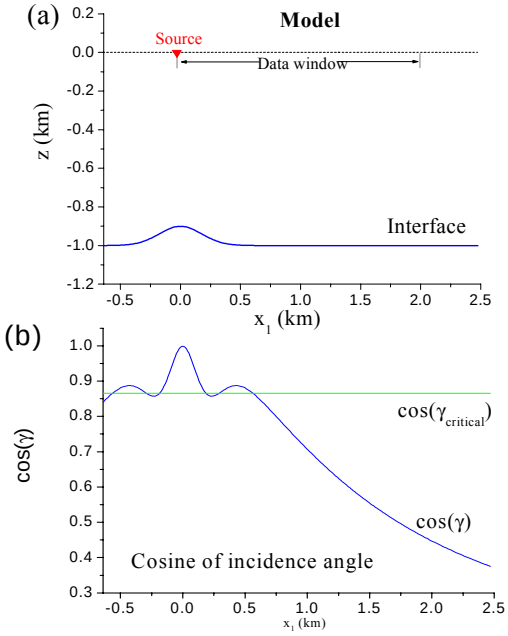


Figure 7: Reflection at an interface with an anticline (Test 3).

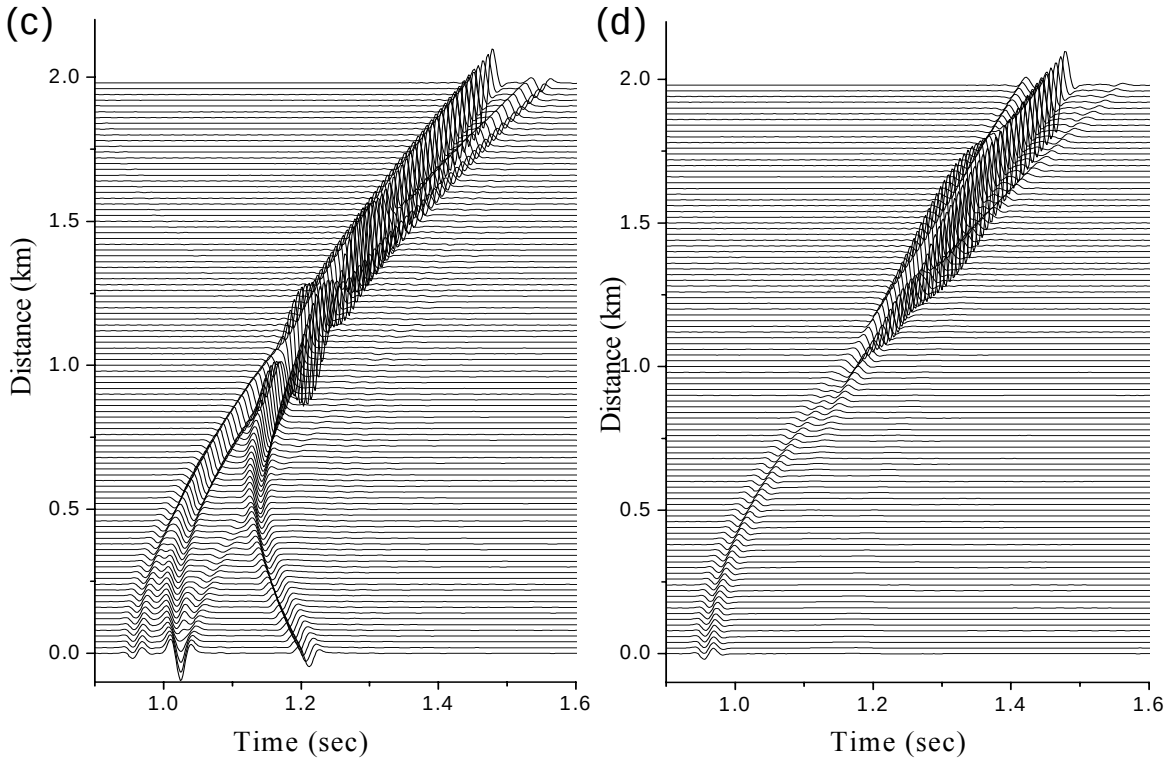


Figure 7 (cont.): Comparison of seismograms obtained using the plane-wave reflection coefficient (c) and the effective reflection coefficient (d) in the anticline interface model (a b) (Test 3)

visible in (c) but is partly masked by the primary reflection. The chosen receiver distribution cannot detect other headwaves from the overcritical strip $-0.242 < x_1 < -0.075$ km on the syncline part of the interface. We notice that this headwave moves from one side of the syncline part to its opposite side and causes secondary scattering, which is a topic beyond the scope of this report. Strong artificial edgewaves from two inner critical contours (radii 0.075 km and 0.242 km) are also visible.

Test 3. The third test is devoted to reflection from an anticline type curvilinear interface given by the expression $z = -1 + 0.1\exp\left\{-16\left(x_1^2 + x_2^2\right)\right\}$ km. Again, the velocities of the two layers are $c_1 = 2$ km/s and $c_2 = 4$ km/s, respectively. For this test we use the same distribution of receivers as in Test 2. The model and cosine of the incidence angle are shown in Figure 7. From the cosine graph it follows that three circles of critical points appear on the interface, centred below the source location and with radii of 0.185 , 0.29 and 0.566 km. The corresponding seismograms (Figure 7 c, d) contain only one event of a pure reflection wave, which is relatively weak in the interval $0 < x_1 < 1.0$ km but has a significant amplitude at far-offset ($1.0 < x_1 < 2.0$ km), corresponding to the overcritical zone $0.566 < x_1 < 1.0$ km at the interface. The seismogram obtained by using the plane-wave reflection coefficient (c) is severely distorted by the artificial diffractions, while the seismograms obtained using the effective reflection coefficient (d) can easily be interpreted in terms of reflections and headwaves.

Two headwaves are well defined. The first headwave arrival is generated in the overcritical zone $0.566 < x_1 < 1.0$ km, confined to the plane part of the interface. This event is visible in interval $1.14 < x_1 < 2.0$ km and is the same headwave that appears for the syncline model in Figure 6d.

The second headwave arises from the overcritical strip $0.185 < x < 0.29$ km and has strong focusing at the point $(0.98, -0.247$ km$)$

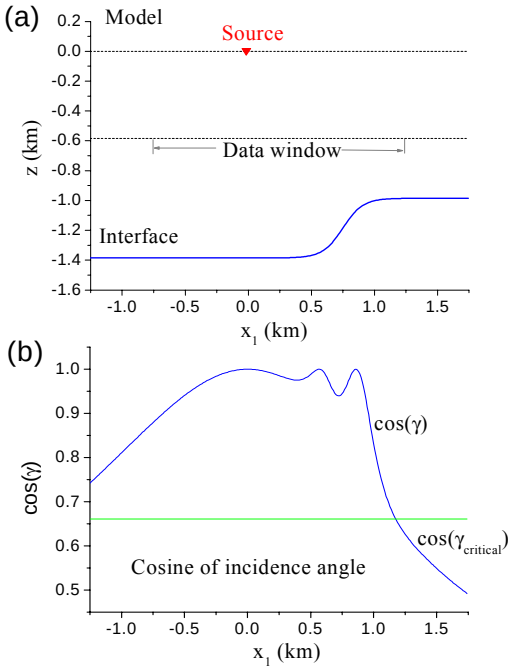


Figure 8: Reflection at a tanh-like interface [7]. (Test 4).

where the Gaussian bell changes curvature and where the headwave rays form a caustic. The associated triplication can be seen in the seismogram, the first branch as a strong event with low apparent velocity is visible on the interval $1.4 < x_1 < 2.0$ km, and the second branch is a weaker event visible between the primary reflection and first branch. A third event is formed in the caustic shadow visible at offsets from 0.8 to 1 km.

Test 4. The model for this test is chosen to enable the caustic response to be properly recorded by the receivers. We consider a tanh-like interface using the expression $z = -1.185 + 0.2 \tanh\{2\pi(x_1 - 2)\}$ km and the velocities $c_1 = 3$ km/s and $c_2 = 4$ km/s, which is identical to the model used in [7]. As shown in Figure 8a, the receivers are horizontally distributed at intervals of 0.02 km from the point with coordinates $(-0.75, 0, -0.585 \text{ km})$ to the point with coordinates $(1.25, 0, -0.585 \text{ km})$. As shown in Figure 8b, there is a contour of critical points intersecting the projection of the profile at distance 1.06 km. The seismograms in Figure 8c,d contain pure reflections including a caustic formed by the reflected waves from the concave interface between the two points of normal incidence $x_1 = 0.593$ km and $x_1 = 0.832$ km.

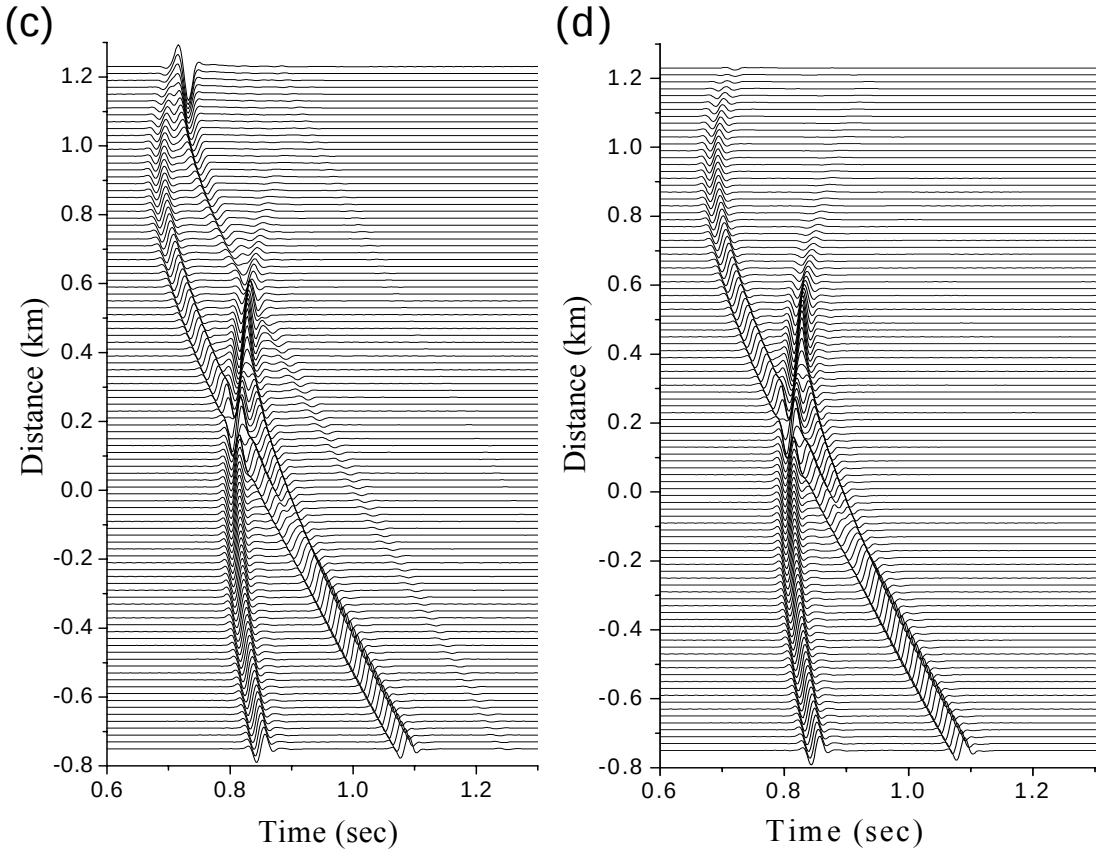


Figure 8 (cont.): Comparison of seismograms obtained using the plane-wave reflection coefficient (c) and the effective reflection coefficient (d) in the tanh-like interface model (a,b) . (Test 4).

Although the critical angles are contained in the model (b), the associated events arrive beyond the present receiver array (a), except for the corresponding artificial diffraction in (c) approaching from far-offset due to the discontinuity of the plane-wave reflection coefficient at the critical reflection point (1.06 km). The features of the reflection triplication of the P-wave obtained by complex ray tracing and finite difference modelling in [7] are well reproduced in (d).

6. Formation of headwave caustics by the concave part of a Gaussian bell.

In the previous experiments we have demonstrated the capability of the new TWSM algorithm to handle correctly critical and super-critical reflections as well as headwaves. Examples of headwave caustics and reflection caustics are also shown. The experiment in this section demonstrates in more detail the development of headwaves and headwave caustics at the slope of a Gaussian bell, as the slope and curvature changes with the height of the bell. We consider a Gaussian-type interface similar to the one we used in Test 3, but given by the expression

$$z = -1 + \Delta z \exp\left\{-16\left((x_1 - 0.92)^2 + x_2^2\right)\right\} \text{ km}$$

with the parameter Δz varying its shape (Figure 9). Here we consider density contrast $\rho_1/\rho_2 = 1$ and velocities $c_1 = 2$ km/s and $c_2 = 8$ km/s are chosen to provide better separation between the headwaves and the reflected wave in the seismogram. The model shown in Figure 9 has 80 receivers that are distributed at intervals of 0.05 km in the level $z = 0$, on either side of apex of the Gaussian bell, but with the source point coinciding with the first receiver to the left. Graphs of the cosines of the incidence angles for four different values of the bell height: $\Delta z = 0.005, 0.02, 0.04, 0.08$ km are shown in (b). Figure 10 shows the corresponding seismograms computed by TWSM using the effective reflection coefficient. We discuss the seismograms in order of increasing value of Δz.

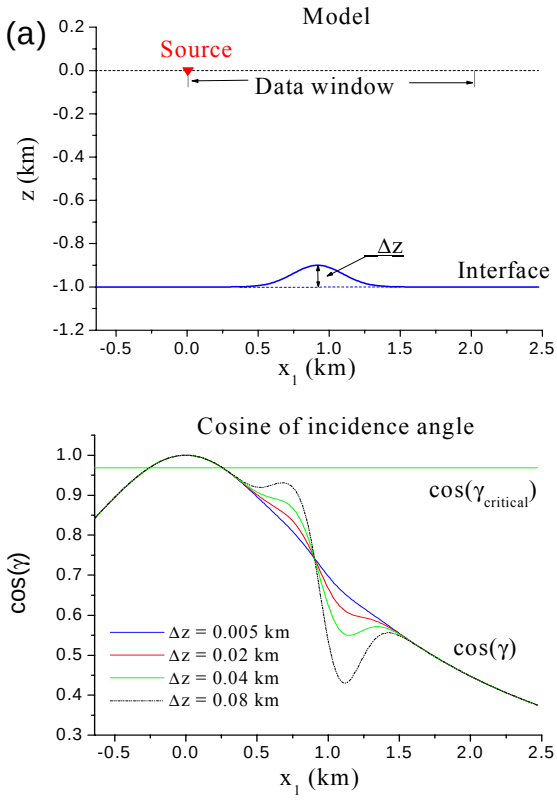


Figure 9*:* Reflection at a Gaussian anticline of varying height. Formation of headwave caustics.

For $\Delta z = 0.005$ km the headwave is well developed. Reflected wave amplitudes increase with increasing values of Δz, or increasing curvature of slope in the interval $(0.5, 0.75\,\text{km})$. A bright event starts to develop at $\Delta z = 0.02$ km in the pure reflected arrival in the interval $(0.5, 1.0\,\text{km})$ at traveltime from 1.1 to 1.2 s. Two headwave branches are seen to develop and intersecting at a caustic event. For $\Delta z = 0.04$ km we clearly see the patterns of the bright reflection event forming a triplication by reflections from the illuminated (left) flank of the Gaussian bell. The branches of headwave arrivals have further developed, and then weakened but still have significant amplitudes for $\Delta z = 0.08$ km. Because the headwave front is propagating from the concave part of the right flank, with a negative curvature, the focus of the headwave rays is located between the interface and receiver. When the headwave rays pass through the focus, a loop structure arises in the headwave event in the seismograms.

Conclusions

Comparison of seismograms TWSM obtained with effective coefficients and the exact solution for the case of plane interface reveal that the new TWSM algorithm is sufficiently accurate for most practical applications. We have shown that the TWSM modelling using plane-wave coefficients is not appropriate for wide-angle reflections, near and beyond critical angles. However, the latter applies to any superposition method, where a discontinuity in the wavefield is smoothed by diffraction events. The effective coefficient represents a generalization to non-planar waves, arbitrary interface curvature and arbitrary frequency of the wavelet. We have demonstrated that the present TWSM algorithm provides a complete and accurate representation of a scalar wavefield, including reflection caustics, headwaves and headwave caustics. Since the TWSM is a surface (target) oriented modelling approach its integration in a seismic inversion scheme should be an obvious application.

Acknowledgements

The authors would like to thank the Russian Fund for Basic Research (grants 02-05-06136 and 00-05-65397) and Norsk Hydro ASA, (Bergen, Norway) for support of this study. Helpful remarks from Brian Farrelly are gratefully acknowledged.

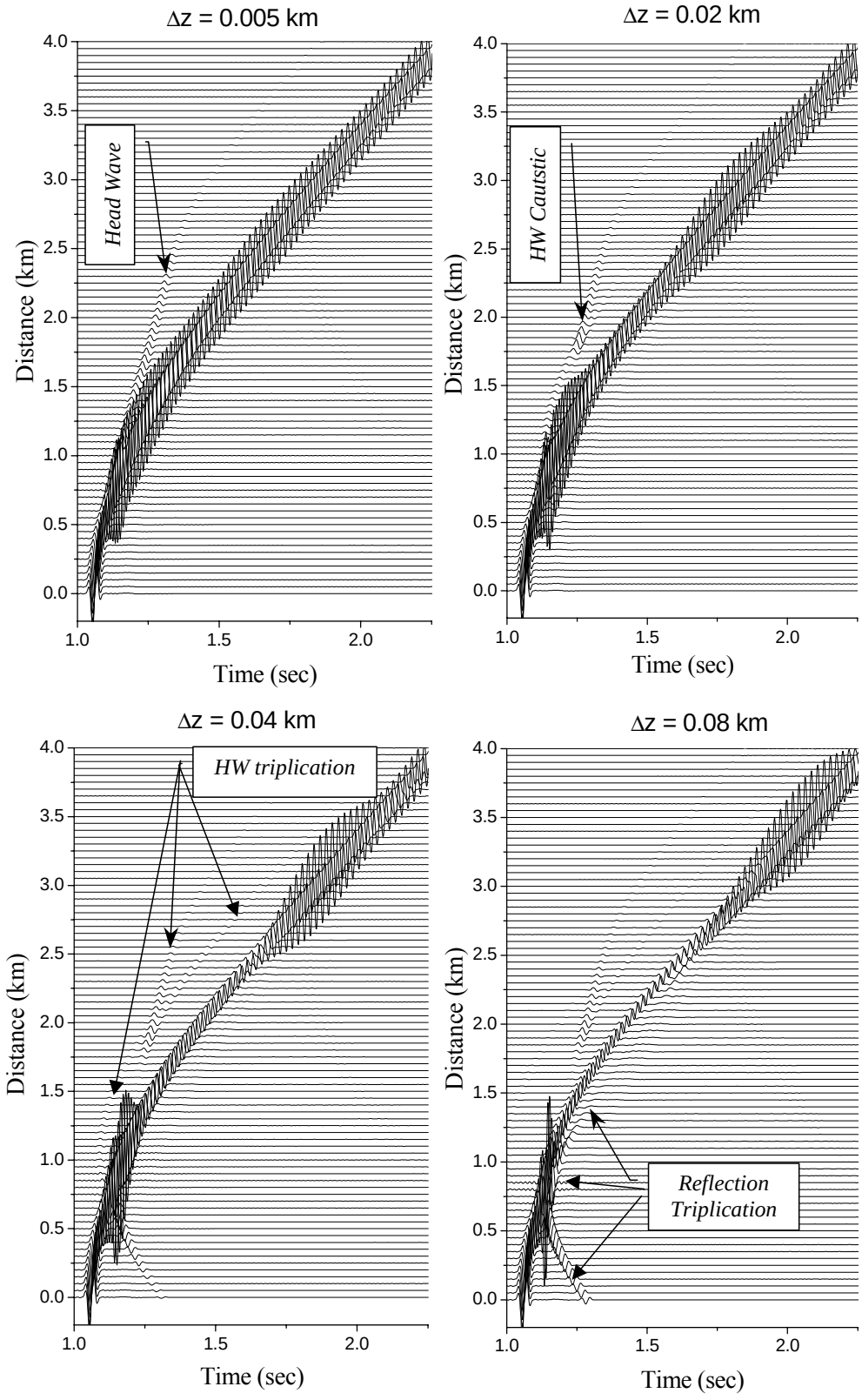


Figure 10: Seismograms obtained by TWSM for the Gaussian anticline with various heights Δz as shown in Figure 9.

References

1. Aizenberg A.M., Klem-Musatov K.D., Pajchel J. and Helle H.B. Seismic simulation by the Tip Wave Superposition method in a complex 3-D model. Norsk Hydro A/S, E & P Research Centre, Bergen (Norway), Open report, 1992.
2. Aizenberg A.M., Helle H.B., Klem-Musatov K.D. and Pajchel J. The tip wave superposition method based on the refraction transform. Extended Abstracts, 58th Meeting, European Association of Geoscientists and Engineers, 1996, Paper C001.
3. Aizenberg, M.A. Research of properties of the transmission operator in transmission problem at plane interface between two homogeneous half-spaces. Bachelor thesis, Novosibirsk State University, 2001.
4. Aizenberg, M.A. Research of properties of the transmission operator in transmission problem at plane interface between two homogeneous half-spaces. Geophysical Bulletin, 2002, No. 1, 10-12 (in Russian).
5. Aizenberg A.M. and Aizenberg, M.A. Simulation of interference field trace reflected/transmitted by plane interface between two acoustic media. Dynamics of solid mechanics, Proceedings of Lavrentiev's Institute of Hydrodynamics SB RAS, V. 119, "Acoustics of inhomogeneous media", Novosibirsk, 2002 (in Russian, to be printed).
6. Goldin S.V. Estimation of reflection coefficient under migration of converted and monotype waves. Russian Geology and Geophysics, 1992, V. 33, No. 4, 76-90.
7. Hanyga A. & Helle H.B. Synthetic seismograms from generalized ray tracing. Geophys. Prosp., 1995, V. 43, 51-75.
8. Klem-Musatov K.D., Aizenberg A.M., Pajchel J. & Helle H.B. Edge and tip diffractions (Theory and Applications in Seismic Prospecting). Lecture notes, University of Bergen, Bergen, 1994.
9. Klem-Musatov K.D., Aizenberg A.M., Helle H.B. & Pajchel J. Reflection and transmission at curvilinear interface in terms of surface integrals. Wave Motion, 2002 (submitted).
10. Roach G.F. Scattering from unbounded surfaces. Proceedings of Dundee Conference, Pitman Research Notes, 1993, 248-272, Longmans, London.
11. Sen M.K. & Frazer L.N. Multifold phase space path integral synthetic seismograms. Geophys. J. Int., 1991, V. 104, 479-487.
12. Treitel S. & Lines L. Past, present and future of geophysical inversion – A new millennium analysis. Geophysics, 2001, V. 66, 21-24.

13. Wenzel F., Stenzel K.-J. & Zimmermann U. Wave propagation in laterally heterogeneous layered media. Geophys. J. Int., 1990, V. 103, 675-684.
14. Zhang Bo. On transmission problems for wave propagation in two locally perturbed half-spaces. Math. Proc. Camb. Phil. Soc., 1994, V. 115, No. 3, 545-558.